Journal of Materials Science: Materials in Electronics (2020) 31:6547–6559
https://doi.org/10.1007/s10854-020-03211-2

Effect of bismuth–tin composition on bonding strength of zinc particle–mixed copper nanoparticle/bismuth–tin solder hybrid joint

Toshikazu Satoh[1] · Masanori Usui[1]

Received: 17 December 2019 / Accepted: 5 March 2020 / Published online: 13 March 2020
© Springer Science+Business Media, LLC, part of Springer Nature 2020

Abstract
In this study, the effect of Bi–Sn composition on the bonding strength of Zn-mixed hybrid joints composed of SiC/Cu and SiC/direct bonded copper (DBC) was examined. For both joints, the bonding strength exhibited a similar dependence on Bi–Sn composition, and the maximum strength obtained for the average Bi fraction in the Bi–Sn alloy particles was 38.2 wt%. This composition is more Sn-rich than the eutectic composition of the Bi–Sn alloy. The bonding strength of the SiC/Cu joints was lower than that of the SiC/DBC joints throughout the entire Bi–Sn alloy composition range. The degree of Bi segregation at the interfacial region decreased with a decreasing Bi fraction in the Bi–Sn particles and was correlated with the bonding strength for the Bi fraction below 38.2 wt%. Defects such as voids and cracks were also observed in the bonding layer, which were likely a result of the difference in the bonding strengths between the SiC/Cu and SiC/DBC joints. Furthermore, delamination of the bonding layer at the interface was observed in the joint that had Sn particles as the starting material. These results indicate that Zn mixing in the hybrid joint enables the reduction of the Bi fraction of the Bi–Sn alloy, leading to improved bonding strength.

1 Introduction

The recent rapid popularization of electrically powered vehicles has led to the increased demand for the development of power control units with much higher efficiency. The efficiency of a power semiconductor device plays a key role in determining the efficiency of the power control unit and thus must be improved. To date, Si-based power devices have been used as power semiconductors in power control units. While the efficiency of the Si-based power devices has improved over the past several decades, it is rapidly approaching the limit of the performance possible in a Si-based device. Therefore, novel power semiconductor devices based on compound semiconductors such as SiC and GaN have attracted the attention of researchers in recent years [1–3]. The high cost of compound semiconductor devices compared to the currently used Si-based devices has motivated a research effort aimed at the downsizing of power devices. Such downsizing will result in an increased current density through the devices that will be accompanied by an increase in the device temperature. While the compound semiconductor devices can be driven even at a temperature as high as 573 K [4–6], the lack of thermal durability of the components surrounding the compound semiconductor device has hindered the further development of this technology.

Bonding materials that join the devices and the lead frames are strongly affected by the heat from the power semiconductor device. To date, Sn-based solder has been used for such joints because it meets the requirement of low toxicity [7–9]. However, because of its low melting point, the Sn-based solder has poor thermal durability when the operational temperature of the power semiconductor device rises as a result of increased current density. High heat-durable bonding materials have therefore attracted more attention in recent years, and many studies have been carried out on various bonding materials [10–26]. In our previous work, we proposed the use of Cu nanoparticle/ Bi–Sn solder hybrid bonding for such bonding [27]. This hybrid bonding combines the wettability of soldering and thermal durability of nanoparticle bonding; while the interfacial wettability is obtained by the melting of the Bi–Sn solder in primary firing at a lower temperature, the bonding layer with high thermal durability is constructed by the sintering of the Cu nanoparticles and the Cu–Sn reaction in the main firing at

✉ Toshikazu Satoh
toshi@mosk.tytlabs.co.jp

[1] Toyota Central R&D Labs., Inc., 41-1 Yokomichi, Nagakute, Aichi 480-1192, Japan

a higher temperature. Although hybrid bonding is similar in bonding method to transient liquid-phase sintering, we have distinguished between them because hybrid bonding involves solid-state sintering of Cu nanoparticles to improve thermal durability, and liquid-phase Bi remains throughout the firing process.

In previous works, we used Bi–Sn solder particles in their eutectic composition (Bi-43 wt% Sn) for the studies of the hybrid joint. This is because our preliminary studies (Fig. 1) revealed that the maximum bonding strength was obtained when the eutectic Bi–Sn particles were used. In this study, we examine the influence of the Bi fraction in the Bi–Sn particles on the bonding strength of the Cu nanoparticle–30 wt% Bi–Sn particle hybrid joint composed of SiC and a Cu/Si_3N_4/Cu stacked plate (DBC: direct bonded copper) fired at 623 K under the application of several different pressures. However, the Bi-rich phase segregates at the interfacial region in the hybrid joint, leading to a loss of the bonding strength and reliability of the joint. The interfacial segregation of the Bi-rich phase was observed in previous studies of Bi–Sn solder, where it was shown to be decreased by the mixing of other elements because of the growth of intermetallic compounds at the interface [28–31]. Our previous studies revealed that the conditions of the primary firing and the particle size of the Bi–Sn particles affect the degree of interfacial Bi segregation and the bonding strength by increasing the amount of Sn-based intermetallic compound at the interface [32, 33]. However, a decrease in the total content of Bi in the bonding layer is favorable because of the poor thermal and mechanical characteristics of Bi-containing phases. Our recent study indicated that the mixing of Zn particles into the mixed Cu nanoparticle/Bi–Sn particle paste enhances the bonding strength of the hybrid joint [34]. We also found that because of the Zn mixing, interfacial Bi segregation was suppressed, and the amount of the Bi-rich phase that did not contribute to the bonding increased. These results imply that Zn mixing enhances the interfacial wettability of the Sn atoms prior to the secondary firing. Therefore, we expect that the bonding strength of the Zn-mixed hybrid joint can be enhanced by using compositions with Sn fractions that are greater than that of the eutectic composition. We report on the influence of the Bi–Sn composition on the bonding strength of the Zn-mixed hybrid joints.

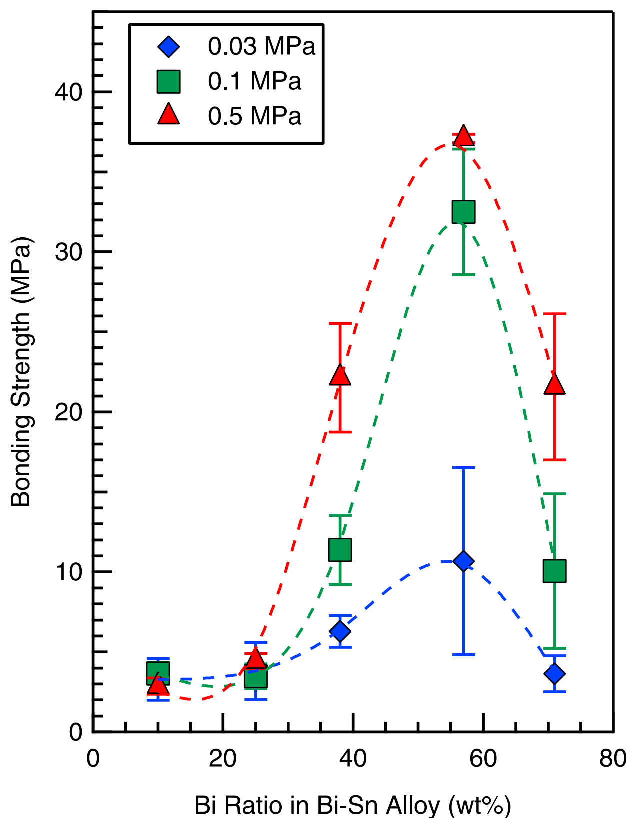

Fig. 1 Influence of Bi fraction of the Bi–Sn particles on the bonding strength of the Cu nanoparticle/30 wt% Bi–Sn particle hybrid joint composed of SiC and DBC subjected to firing at 623 K and the application of several additional pressures

2 Experimental procedure

The SiC/Cu and SiC/DBC joints schematically shown in Fig. 2 were prepared in this study. The components of the joints included 4H-SiC (0001) chips with the dimensions $5 \times 5 \times 0.35$ mm^3 (purchased from TankeBlue), O-free Cu plates with the dimensions $20 \times 20 \times 3$ mm^3, and DBC plates composed of 0.32-mm-thick Si_3N_4 plates placed between 0.15-mm-thick pieces of Cu foil with the dimensions 20×20 mm^2 (purchased from Denka). (Although the stacked plates are not manufactured by the direct bonding method but by active metal brazing, we have denoted them by "DBC" herein.) As adhesive layers, multilayered films with the Ag (100 nm)/Ni (1 µm)/Ti (100 nm) structure were deposited onto the SiC chips, and Ag (100 nm)/Ni (1 µm) films were deposited onto the Cu and DBC plates by radio frequency magnetron sputtering (Tokuda CFS-8EP-55). The structure of the adhesive layers exhibits sufficient interfacial strength to adhere to both the substrates and the Cu nanoparticle bonding layer [35, 36].

The mixed particle paste for the formation of the Zn-mixed hybrid joints was prepared as follows. Cu nanoparticles with an average size of 230 nm (surface-modified using decanoic acid and decylamine) were synthesized according to a previously described procedure [9, 13]. Eutectic Bi-43 wt% Sn alloy particles with an average diameter of 10 µm were purchased from CuLox Technologies. Bi-75 wt% Sn and Bi-90 wt% Sn particles with a diameter of less than 38 µm and Zn particles with an average diameter of 7 µm were purchased from Kojundo Chemical Laboratory. Sn

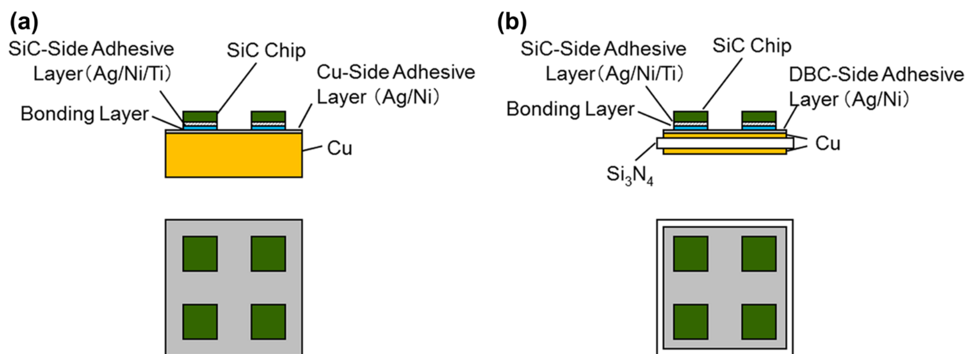

Fig. 2 Schematic of **a** SiC/Cu and **b** SiC/DBC joints

Table 1 Mixing ratios of Cu, Bi–Sn, Sn, and Zn particles in pastes A–D

Paste	Mixing ratio (wt%)						Bi ratio in all Bi–Sn (wt%)	Bi ratio in all particles (wt%)
	Cu	Bi − 43 wt% Sn	Bi − 75 wt% Sn	Bi − 90 wt% Sn	Sn	Zn		
A	55	25	0	0	0	20	57	14.3
B	55	15	10	0	0	20	44.2	11.1
C	55	15	0	10	0	20	38.2	9.6
D	55	15	0	0	10	20	34.2	8.6

particles with an average diameter of 10 µm were purchased from Sigma-Aldrich. The Cu, Bi–Sn, and Zn particles were mixed in 1-decanol using a planetary centrifugal mixer to obtain the mixed particle paste, and the mixing rates of these particles are shown in Table 1. During this procedure, 70 µl of the solvent was used per 1 g of the mixed particles.

A layer of the mixed particle paste with an area of 5 × 5 mm^2 and a thickness of 0.1 mm was printed on the adhesive-layer-modified Cu or DBC plate using a metal mask, and then the SiC chips were stacked onto the paste layer with the adhesive layer facing down. The entire stack of the SiC chips, adhesive layer, mixed particle paste layer, and Cu or DBC plate was fired in a H_2 atmosphere. The temperature profile for the firing process is shown in Fig. 3. The primary firing steps were performed at 473 K for 20 min and 623 K for 5 min, respectively, and the temperature was increased gradually at a rate of 30 K/min throughout the firing process. In our previous work, we optimized the condition of the primary firing to improve bonding strength through increased interfacial wetting [32], and in our work regarding Cu nanoparticle bonding, we optimized the condition of the secondary firing [35, 36]. A uniaxial pressure of 500 kPa was applied to the bonding region during the firing process. Thickness of the bonding layer that results from this process is in the range of 20–30 µm.

The bonding strength of the produced joints was evaluated with a die-shear test that was performed using a Nordson DAGE 4000Plus bond tester. The height and speed of the shear tool were 50 µm and 50 µm/s, respectively. The average shear strength obtained from the shear strength

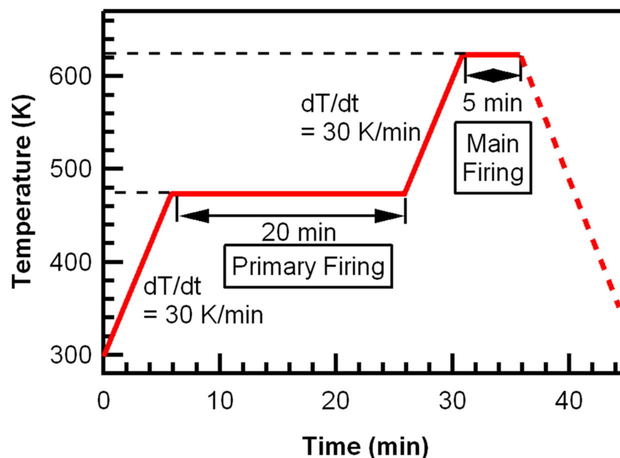

Fig. 3 Temperature profile of the firing process

measurements of the three joints is defined as the bonding strength. Scanning electron microscopy (SEM) of the joint cross sections was performed using a Hitachi S-3600N SEM at an accelerating voltage of 10 kV. Elemental mapping analysis by energy-dispersive X-ray spectroscopy (EDS) was performed using a Horiba EMAXEvolution EX-370X system with a Hitachi SU3500 SEM at an accelerating voltage of 15 kV.

X-ray diffraction (XRD) measurements were performed in the θ–2θ configuration using a Rigaku Ultima-IV XRD system to identify the constituent phases of the bonding layer. Two glass (Corning Eagle XG) plates were bonded

following the above-described procedure using Paste A. One glass plate with the dimensions $20 \times 20 \times 0.7$ mm^3 was coated with Ag (100 nm)/Ni (1 μm)/Ti (100 nm), and another glass plate with the dimensions $6 \times 6 \times 0.7$ mm^3 was coated with Ag (100 nm)/Ni (200 nm). The die-shear test was performed on the glass joint, and the fracture plane was analyzed by XRD. The X-ray source was Cu-Kα and its accelerating voltage and tube current were 40 kV and 40 mA, respectively.

3 Results and discussion

Figure 4 shows the measured bonding strengths of the SiC/Cu and SiC/DBC joints plotted versus the mass fraction of Bi in the Bi–Sn alloy in the paste. The bonding strength of the SiC/DBC joints was higher than that of the SiC/Cu joints for the same mass fraction of Bi. The bonding strengths of the SiC/Cu joints and the SiC/DBC joints showed similar dependences on the Bi mass fraction. The bonding strength first increased with increasing Bi fraction up to 38.2 wt% Bi (Paste C), which is a more Sn-rich composition than the eutectic point composition. Thereafter, as the Bi fraction increased further, the bonding strength decreased gradually

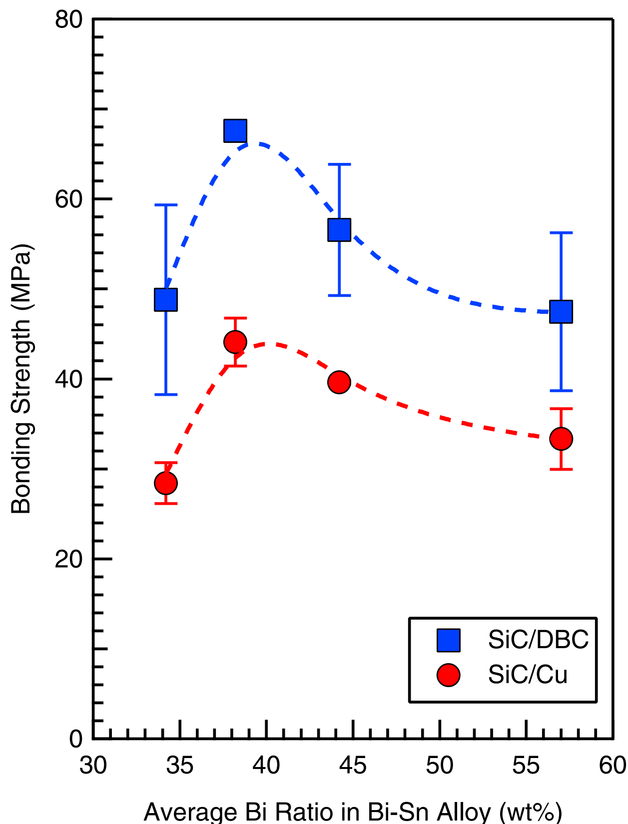

Fig. 4 Bonding strengths of SiC/Cu and SiC/DBC joints versus the mass fraction of Bi in the Bi–Sn alloy

for both joints. The maximum bonding strength values were 44.1 and 67.2 MPa for the SiC/Cu and SiC/DBC joints, respectively.

Cross-sectional SEM micrographs of the central region and the edge region in the bonding area of the SiC/Cu joints are shown in Figs. 5 and 6, respectively, with the region shown in the brightest contrast corresponding to the Bi-rich phase. The amount of the Bi-rich phase decreased with the decrease in the Bi-mixing ratio of the mixed particle paste, and most of the Bi-rich phase segregated in the interfacial region. The degree of interfacial segregation also decreased with increasing Bi-mixing ratio, and it was larger in the edge region than in the central region. Defects such as voids, cracks, and interfacial delamination were observed around the bonding layer. The observed voids are classified into two groups by their sizes. The diameter of the larger voids was about 10 μm, and the diameter of the smaller voids was less than 3 μm. There was little systematic dependence of the amount of the formation of larger voids, cracks, and interfacial delamination sites on the Bi-mixing ratio. However, the number of smaller voids exhibited opposite correlation with the Bi-mixing ratio. On the other hand, a regional dependence of the amount of the defects was observed. Many voids, cracks, and interfacial delamination sites were observed in the edge region, as shown in Fig. 6. By contrast, even though several voids were observed, as shown in Fig. 5a–c, generally there were few cracks and little interfacial delamination in the central region with the exception of the interfacial delamination that was observed in the joint using Paste D as shown in Fig. 5d.

Cross-sectional SEM micrographs of the central region and the edge region in the bonding area of the SiC/DBC joints are shown in Figs. 7 and 8, respectively. The segregation of the Bi-rich phase at the interfacial region was also observed in these joints, as shown in Figs. 7 and 8. The degree of the segregation in the edge region shown in Fig. 8 was larger than that in the central region shown in Fig. 7, as observed in the SiC/Cu joints shown in Figs. 5 and 6. However, the amount of the interfacial segregation of the Bi-rich phase in the SiC/DBC joints was much smaller than it was in the SiC/Cu joints. Likewise, defects such as larger and smaller voids, cracks, and interfacial delamination were also observed in the bonding layer of the SiC/DBC joints, albeit in much smaller amounts than in the SiC/Cu joints. More defects occurred in the edge region than in the central region, and the smaller voids increased with the decreasing of the Bi-mixing ratio as with the SiC/Cu joints.

Cross-sectional SEM micrographs (back-scattered electron images: BEI) and EDS elemental mapping images of the Cu, Sn, Bi, Zn, Ag, and Ni elements of the SiC/Cu and SiC/DBC joints obtained using Paste C are shown in Figs. 9 and 10, respectively. Little variation was observed in the distribution of the elements between the SiC/Cu and

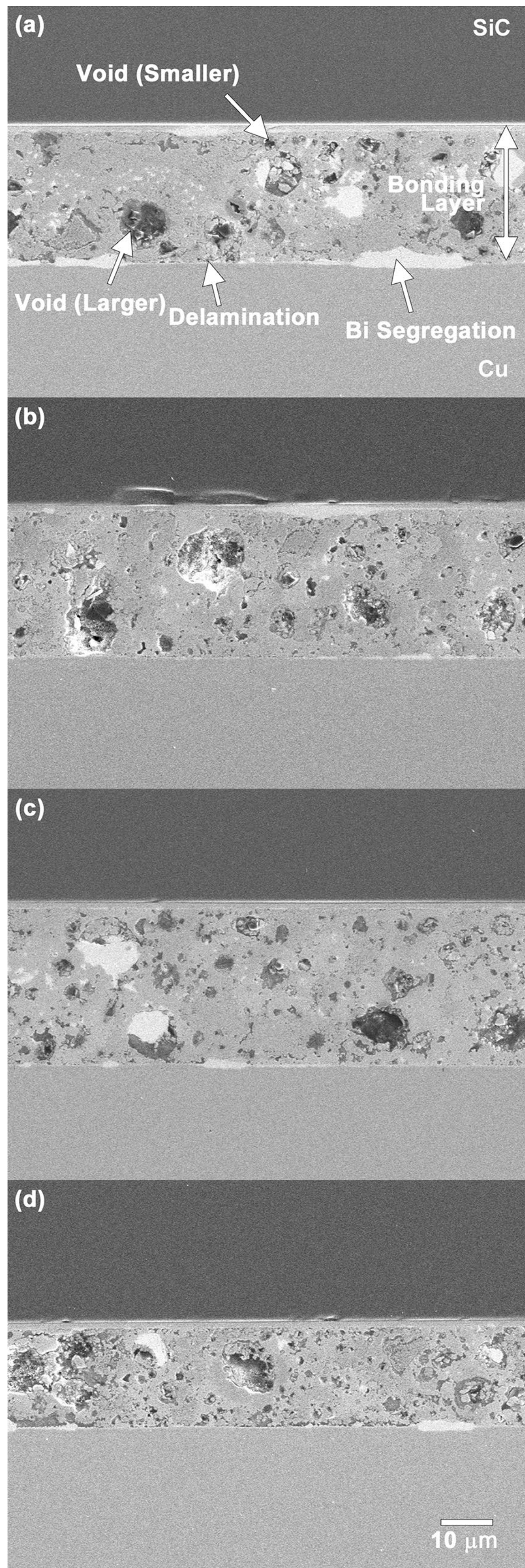

Fig. 5 Cross-sectional SEM micrographs of the central region in the bonding area of the SiC/Cu joints

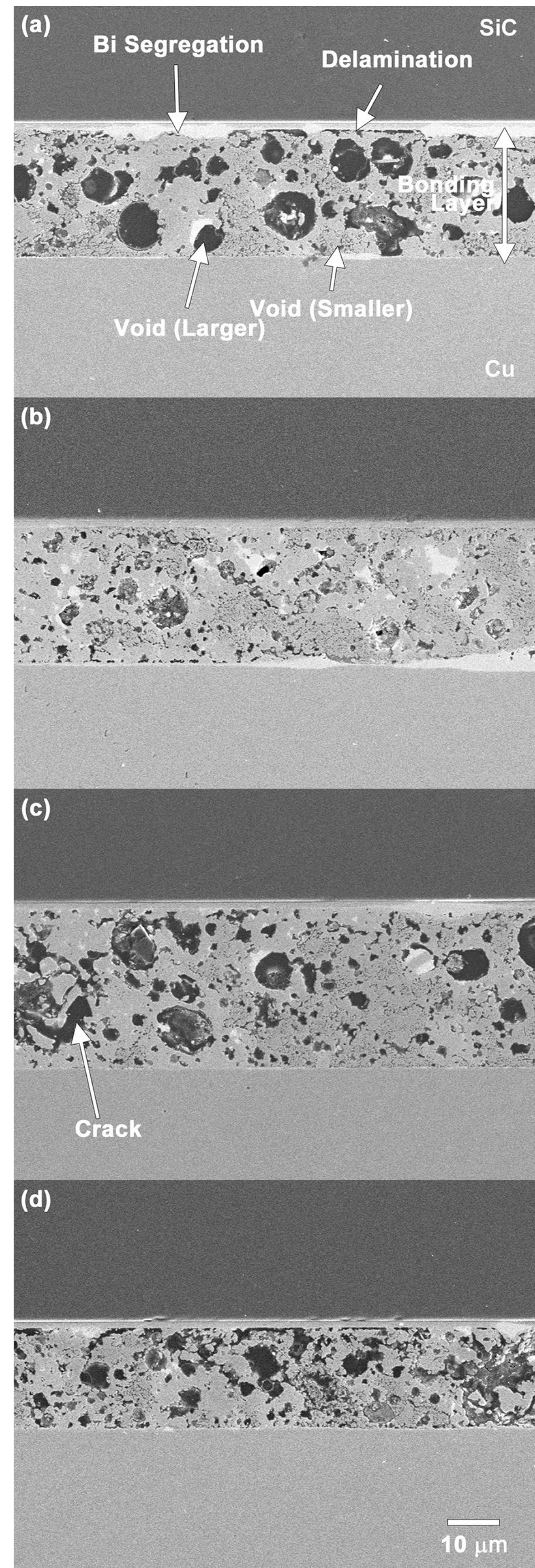

Fig. 6 Cross-sectional SEM micrographs of the edge region in the bonding area of the SiC/Cu joints

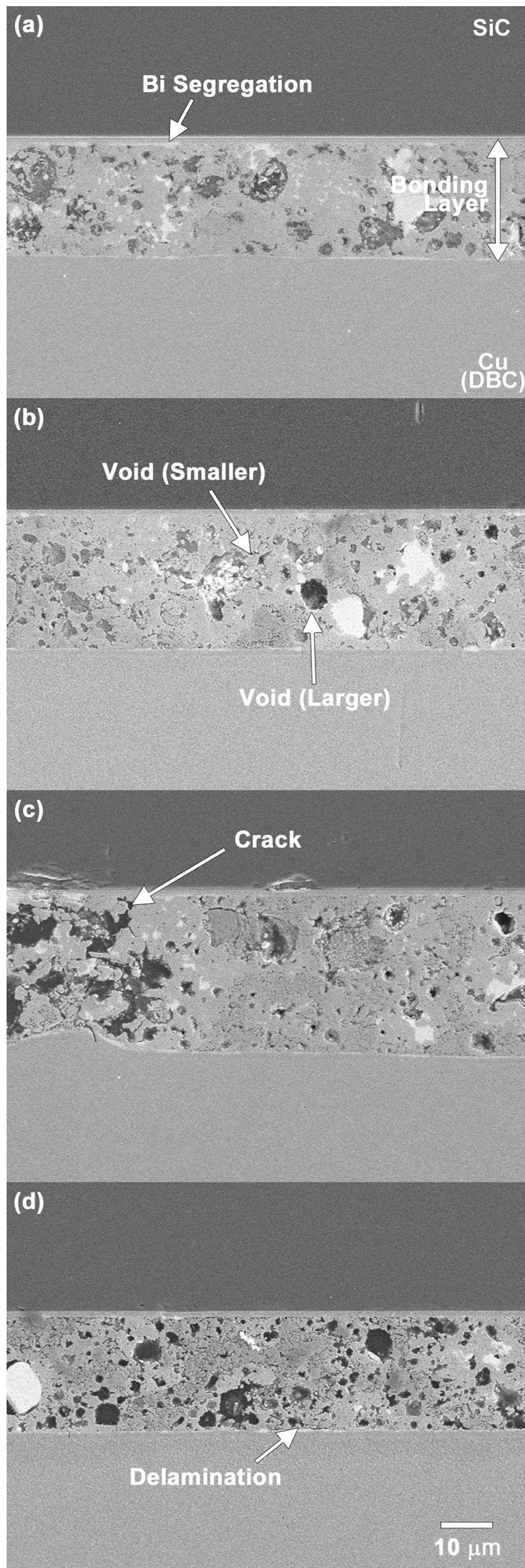

Fig. 7 Cross-sectional SEM micrographs of the central region in the bonding area of the SiC/DBC joints

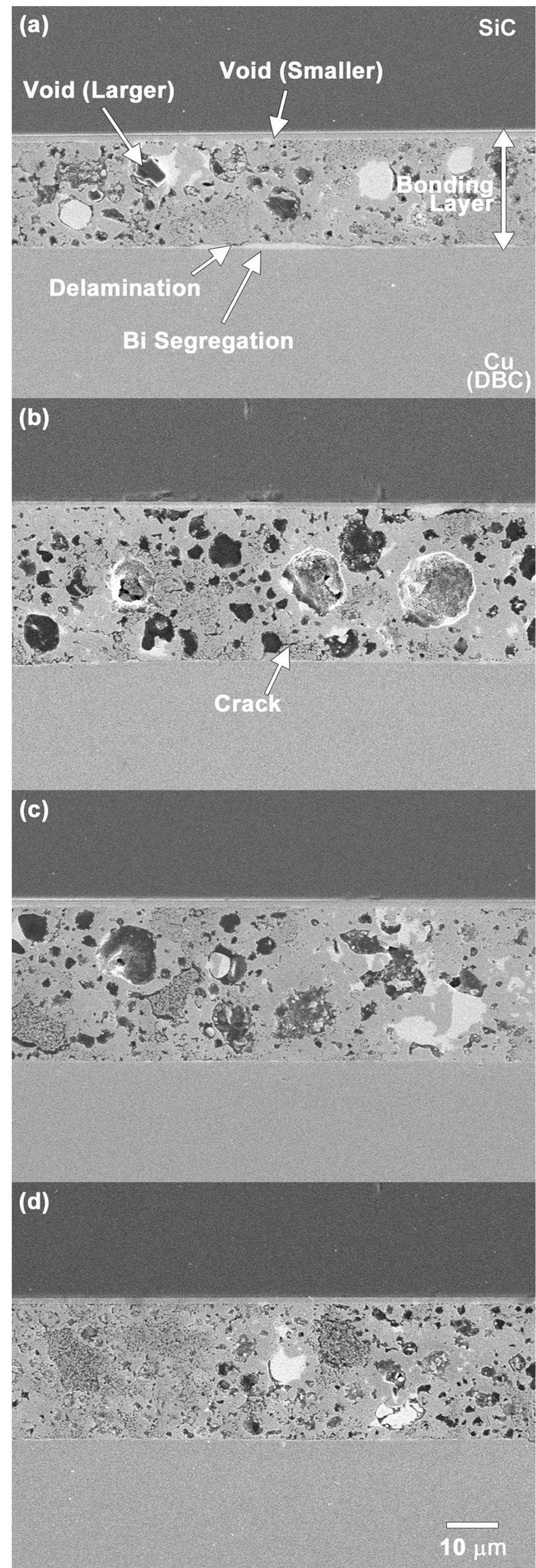

Fig. 8 Cross-sectional SEM micrographs of the edge region in the bonding area of the SiC/DBC joints

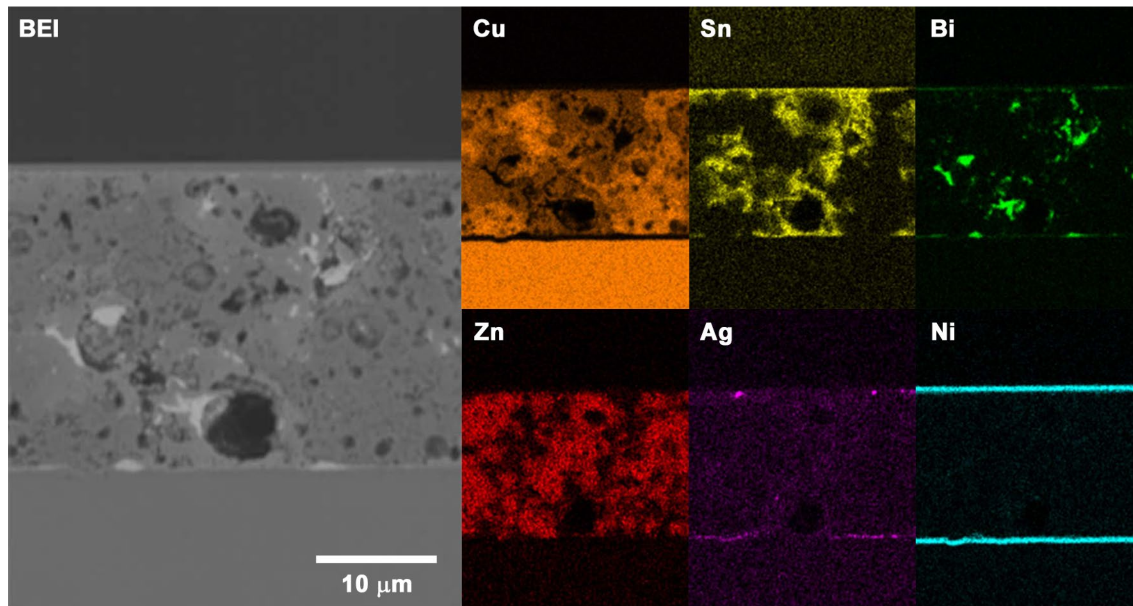

Fig. 9 Cross-sectional SEM micrographs (BEI) and elemental mapping images of Cu, Sn, Bi, Zn, Ag, and Ni by EDS of the SiC/Cu joint obtained using Paste C

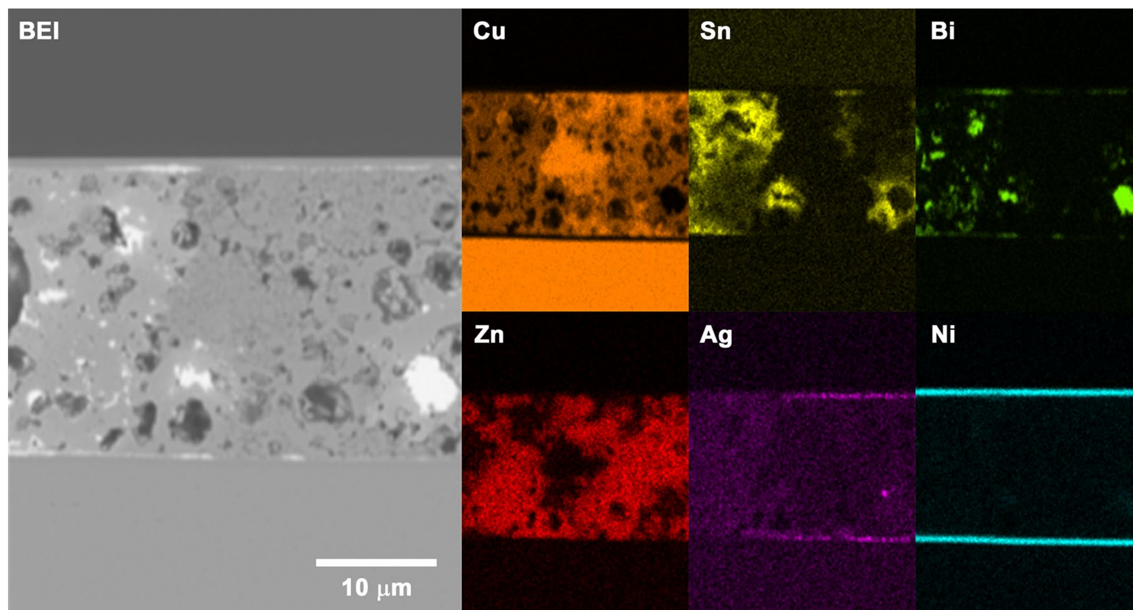

Fig. 10 Cross-sectional SEM micrographs (BEI) and elemental mapping images of Cu, Sn, Bi, Zn, Ag, and Ni by EDS of the SiC/DBC joint obtained using Paste C

SiC/DBC joints. The Zn was widely distributed inside the bonding layer except for the regions composed of voids and the regions with high concentrations of Cu and Bi. The Bi was finely dispersed in the bonding layer, even though some of the Bi formed the interfacial layer. Sn constituted the major part of the bonding layer and wetted the interfacial region, and Sn and Zn coexisted in the same region while showing an inverse linear correlation between their concentrations. At the interfacial region where Sn wetting was observed, the Ag layer disappeared. However, the Ni layer that was deposited below the Ag layer maintained the layer structure even in the presence of the Sn wetting at the interface. These results were similar to the elemental

distribution for the joint obtained using Paste A that was reported in our previous work [34].

The XRD patterns of the bonding layers obtained using Paste A that was fired at 523 K, 573 K, and 623 K for 5 min after firing at 473 K for 20 min are shown in Fig. 11, and the identified phases are listed in Table 2. Only Cu_3Sn was identified as a reaction product in the bonding layer fired at 473 K, and the other identified phases such as Cu, Zn, Bi, Ni, and Cu_2O were derived from the starting materials. It was reported in previous research that Cu_6Sn_5 is the first generating compound in the Cu–Sn system at 473 K prior to Cu_3Sn [16–22]. However, any diffraction line derived from the Cu_6Sn_5 phase was not identified in the pattern. There are two explanations that we have considered for the reason that

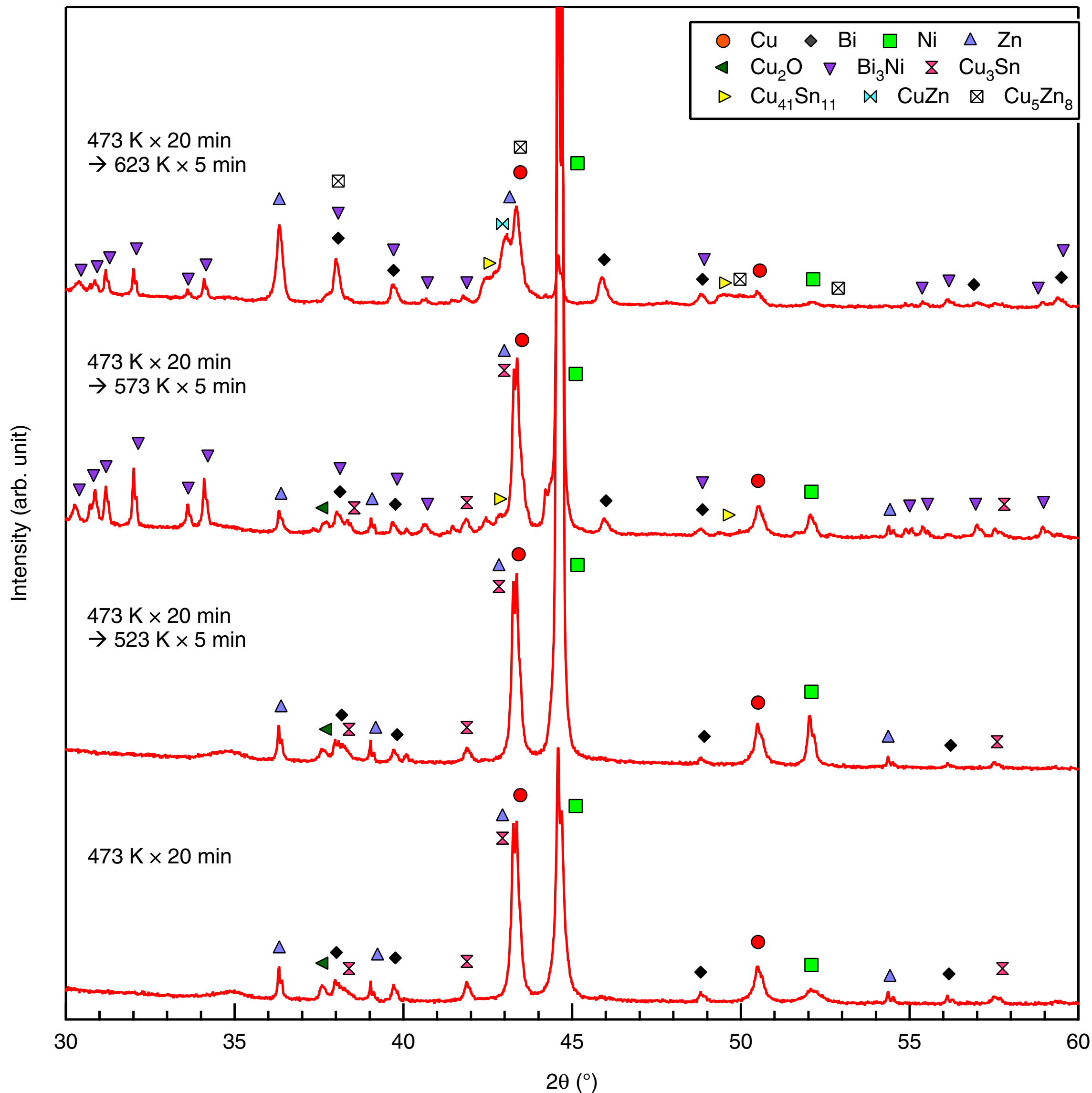

Fig. 11 XRD patterns of the bonding layer using paste A fired at 473 for 20 min followed by firing at 523, 573 and 623 K for 5 min

Table 2 Phases identified in the XRD patterns presented in Fig. 11

Firing condition	Identified phases
473 K × 20 min	Cu, Bi, Zn, Cu_2O, Cu_3Sn, Ni
473 K × 20 min → 523 K × 5 min	Cu, Bi, Zn, Cu_2O, Cu_3Sn, Ni
473 K × 20 min → 573 K × 5 min	Cu, Bi, Zn, Cu_2O, Cu_3Sn, $Cu_{41}Sn_{11}$, Ni, Bi_3Ni
473 K × 20 min → 623 K × 5 min	Cu, Bi, Zn, $Cu_{41}Sn_{11}$, CuZn, Cu_5Zn_8, Ni, Bi_3Ni

resulted from high activity of Cu nanoparticles and a limited supply of Sn. One explanation is that the transformation from Cu_6Sn_5 to Cu_3Sn is completed in the primary firing, and the other is that the reaction between Cu and Sn takes place from the Cu side in the Cu–Sn system. It is expected that Cu_6Sn_5 was identified as a first-generated compound in the Cu–Sn system in the literature because of the presence of either or both of the excess Sn supply and the more stable surface of the balk Cu compared with the Cu nanoparticle. There was little difference in the composing phases after firing at 523 K for 5 min compared to the phases after firing at 473 K for 20 min. When the firing temperature was raised to 573 K, Bi_3Ni and $Cu_{41}Sn_{11}$ were newly generated. While the Cu_3Sn and Cu_2O disappeared, additional reaction products composed of Cu and Zn such as CuZn and Cu_5Zn_8 were identified in the bonding layer fired at 623 K. The only Cu–Sn compound identified in this bonding layer was $Cu_{41}Sn_{11}$. Figure 12 shows the cross-sectional SEM micrograph (BEI: back-scattered electron image) and EDS elemental mapping images of the Cu, Sn, Bi, Zn, Ag, and Ni elements of the SiC/DBC joints obtained using Paste A fired at 473 K for 20 min. The images indicate that Sn coexisted with Cu in a significant portion of the bonding layer. Some of the Ag layer no longer formed at the locations where Sn arrived at the interface, whereas Ni retained its layer structure. The Bi stayed inside the bonding layer in the form of spherical grains that appeared with the brightest contrast in the BEI without mixing of the other elements. The region of high Zn concentration corresponds to the region with the dark contrast in the bonding layer in the BEI. While most of the Zn is present in the form of spherical grains, some Zn particles with an indeterminate shape were also found in the region indicated in “A” in the BEI, indicating they were coexisting with Cu. Regions composed of Cu and Sn were observed inside some spherical Zn grains in the region labeled “B.” Additionally, because the contours of the elemental mapping image of the Zn were not clear compared to the other elements, Zn is likely to be dispersed at a low concentration throughout the entire bonding layer. Figure 13 shows the cross-sectional BEI and EDS elemental mapping images of the Cu, Sn, Bi, Zn, Ag, and Ni elements of the SiC/DBC joints obtained using Paste A fired at 473 K for 20 min followed by firing at 573 K for 5 min. Although some of the Bi maintained a spherical grain shape in the bonding layer, some of the Bi migrated to the interfacial region and segregated, as shown by the region labeled “C.” In that region, the Ag layer disappeared, and the shape of the Ni layer became indistinct. Although little difference was confirmed in the feature of the elemental contribution of Cu, Sn, and Zn compared with that shown in Fig. 12, the generation of the Cu–Sn phase in the Zn-phase-like region “D” and the intermixing of Cu and Zn seem to have progressed.

These results indicate that Zn mixing changes the optimum Bi/Sn ratio for hybrid bonding and leads to a higher bonding strength. They also show that for the same Bi/Sn ratio, the bonding strength of the SiC/Cu joints is lower than that of the SiC/DBC joints. We will discuss the mechanism of this effect based on the formation process of the bonding layer.

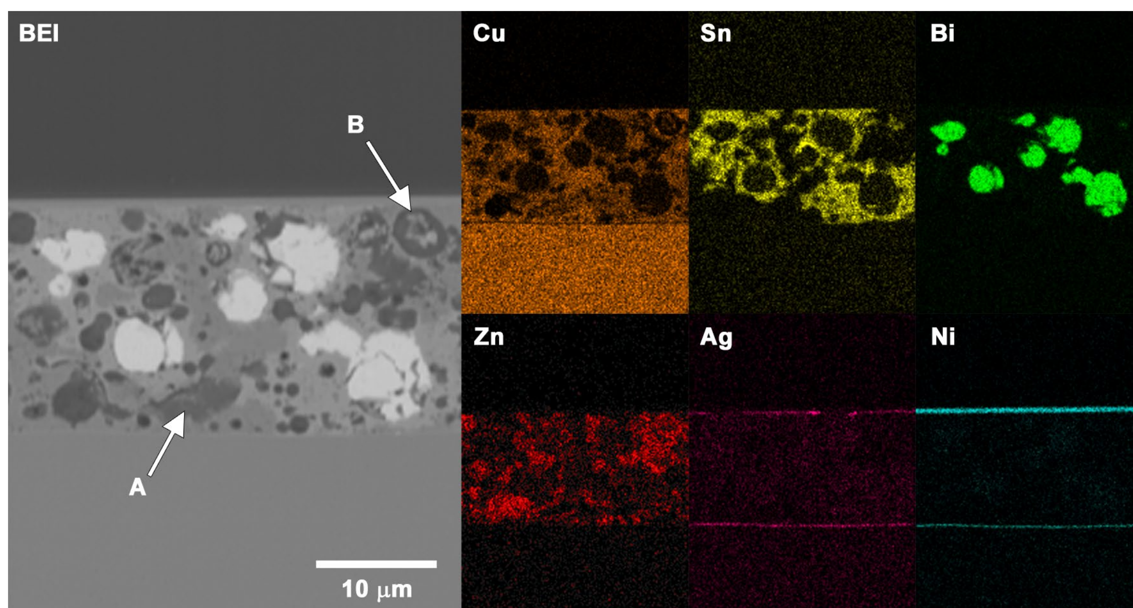

Fig. 12 Cross-sectional SEM micrograph (BEI) and elemental mapping images of Cu, Sn, Bi, Zn, Ag, and Ni by EDS of the SiC/DBC joints using Paste A fired at 473 K for 20 min

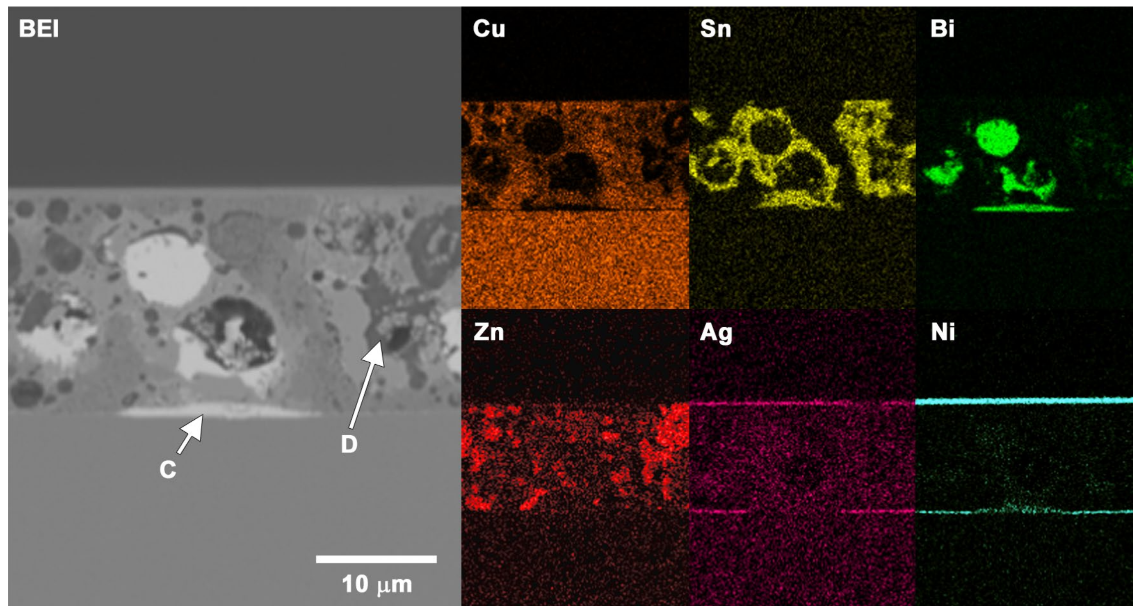

Fig. 13 Cross-sectional SEM micrograph (BEI) and elemental mapping images of Cu, Sn, Bi, Zn, Ag, and Ni by EDS of the SiC/DBC joints using paste A fired at 473 K for 20 min followed by firing at 573 K for 5 min

Phase constitution in the bonding layer, interfacial structure, and the formation of defects are assumed to be important factors that affect the bonding strength. The roles played by these factors as revealed in this work are described below. The SEM images shown in Figs. 5, 6, 7, and 8 suggest that the Bi/Sn ratio does not affect the types of the constituent phases, but it does affect their ratio. The SEM-EDS study revealed that there was little difference in the phase constitution between the SiC/Cu and SiC/DBC joints, while the volume fraction of Bi in the bonding layer decreased with decreasing Bi/Sn ratio. The decrease in the volume fraction of Bi was accompanied by a decrease in the interfacial Bi segregation and an increase in the amount of the Cu–Sn compound. The amount of formation of defects in the bonding layer appears to be independent of the Bi/Sn ratio and is higher in the SiC/Cu joints than in the SiC/DBC joints.

The bonding strength increased with the decrease in the average Bi fraction in the Bi–Sn alloys in both the SiC/Cu and SiC joints for a Bi content of more than 38.2 wt%. The trends for the degree of interfacial Bi segregation are consistent with those found for the above-described important factors. During the primary firing, once the melted Bi phase can be solidified, there is a change in the Bi/Sn ratio caused by migration of the Sn into the bonding layer. The Cu–Sn reaction leads to shrinkage of the bonding layer, whereas the surrounding components expand with the rise in temperature. Therefore, tensile stress is induced in the bonding layer, especially in the interfacial region. In this case, an activation of solid phase diffusion moderates the stress. However, the stress remains in the bonding layer because the diffusion length of the solid-state diffusion is not sufficient to eliminate it. Furthermore, when the temperature rises above the melting temperature of Bi (543 K), liquid-phase Bi migrates to the interfacial region to decrease the stress. Interfacial Bi segregation does not occur in the Bi–Sn solder/Ni interface because of the generation of a stable interfacial Ni_3Sn_4 layer at the interface [37]. However, interfacial wetting of Sn, which is needed for Ni_3Sn_4 generation, cannot take place in the interfacial region in hybrid bonding, because most of the Sn atoms are spent in the Cu–Sn reaction in the bonding layer during the primary firing. Therefore, it is expected that liquid-phase Bi could directly cause the wetting of the Ni surface because of the low eutectic temperature (533 K) of the Ag–Bi system that allows the Bi to easily dissolve the Ag [38]. Additionally, liquid-phase Bi has been reported to penetrate the grain boundary of Ni [39]. However, Bi is considered to be able to penetrate the interface between the Ni layer and the bonding layer, which is considered to require higher energy than the grain boundary, and form the interfacial Bi segregation accompanying the formation of Bi_3Ni.

The above model of the formation of the interfacial Bi segregation is consistent with the results that the formation of the Bi_3Ni phase is observed above 573 K. According to this model, the sites of re-solidified Bi become voids after the migration of the liquid-phase Bi. The size of the larger voids corresponds to that of the spherical Bi grains shown in Fig. 12, and the result also supports the validity of the above-described model of the Bi segregation. Moreover, the observation that the amount of the interfacial Bi segregation differs based on the construction of the joint and the

location in the bonding area is also explained by the model, because the regions with pronounced Bi segregation are the regions which are expected to experience high tensile stress in the firing process. Although interfacial Bi segregation reduces the bonding strength because of the soft and brittle mechanical properties of the Bi-rich phase composed of Bi and Bi_3Ni [40, 41], it increases interfacial wettability in hybrid bonding. Therefore, it is expected that Zn mixing generates alternative interfacial wetting and reinforces the interface to improve the bonding strength, as observed in this study. There are two important mechanisms by which Zn mixing gives rise to the increase in the interfacial wetting. The first is the increased Sn diffusion in the primary firing, and the second is the increase in the wetting area by the Sn-containing compound in the main firing.

First, we will discuss the increase in the Sn diffusion in the primary firing. Diffusion of Sn atoms occurs as reactive diffusion through the Cu phase in the primary firing at 473 K carried out for 20 min in this study, as was also observed in our previous study [32, 33]. This diffusion mode is independent of the Zn mixing. However, Zn addition lowers the liquidus temperature of the Bi–Sn alloy [42]. Therefore, if Zn atoms can dissolve into the Bi–Sn alloy, Zn mixing will increase the amount of the liquid phase and the fluidity of the Bi–Sn alloy in the primary firing. In turn, because of the increased amount of the liquid phase and the fluidity of the Bi–Sn alloy in the primary firing, the activity and access to the interface of Sn atoms can be increased. Furthermore, the Zn mixing can activate the Cu–Sn reaction by lowering the liquidus temperature in Cu–Sn–Zn system [43]. If the Cu–Sn reaction is activated, the diffusion distance of Sn atoms becomes greater. This hypothesis is supported by the morphology of the Zn grains after the primary firing, shown in Fig. 12. Because the interface formed through the reaction with Sn atoms is expected to be strong [44], Zn mixing reinforces the interface because of the increased wetting by the Sn atoms in the primary firing.

Next, we will discuss the increase in the wetting area by the Sn-containing compound in the main firing. Only the Cu_3Sn intermetallic compound was generated in the primary firing, and no Zn-containing compound was identified. After the main firing, Cu_3Sn converted into $Cu_{41}Sn_{11}$, and a reaction between Cu and Zn reaction was identified. At this time, Zn was distributed in the entire bonding layer as shown in Figs. 9 and 10. Furthermore, the CuZn phase can solvate Sn atoms [45]. Therefore, it is expected that Sn atoms diffuse over long distances with reactive diffusion of Zn that occurs in the entire bonding layer when the Cu–Sn compound changes from Cu_3Sn to $Cu_{41}Sn_{11}$. Because the interface is wetted by the Sn atoms at this time, the interface is reinforced, even though Bi segregation that accompanies the formation of Bi_3Ni occurs simultaneously.

On the other hand, the above-mentioned activation of the diffusion and reaction within the bonding layer by the Zn mixing is considered to reinforce the bonding layer. Because the Cu–Sn reaction is limited in the primary firing when the Sn-rich Bi–Sn powder is used, the Cu–Sn reaction would occur at a high rate, and a high quantity of Kirkendall voids, which diminish the bonding strength, would be generated in the bonding layer during the main firing. Since the Zn mixing enables active migration of atoms in the bonding layer in response to the lower temperature, such a drastic reaction could be suppressed, and the density of the bonding layer could be improved. However, Kirkendall voids would be generated by the imbalance of the diffusion within the bonding layer. Such formation of Kirkendall voids is expected to increase with the mixing ratio of Sn, which has the lowest melting point in the bonding layer. It is therefore considered that the smaller voids shown in Figs. 5, 6, 7, and 8 are Kirkendall voids.

Improvement of the bonding strength by Zn mixing, towing to the reinforcement of the interface by increasing Sn wetting and reinforcement of the bonding layer by improving its density, was discussed above. However, the bonding strength of the joint obtained using Paste D, which is the most Sn-rich paste in this study, was lower than those of the other joints, and interfacial delamination was observed. The origin of the low strength of the joints will be discussed below. Table 3 shows the solidus/liquidus temperature of the Bi–Sn alloy particles of the starting material. With the exception of the Sn end member, the solidus temperature of the Bi–Sn alloys is lower than the temperature of the primary firing (473 K). This means that with the exception of Sn, the liquid phase is generated in the Bi–Sn alloy particles even though Bi-90 wt% Sn alloy does not entirely melt because its liquidus temperature is higher than 473 K. Therefore, the above-discussed Sn–Zn interaction in the primary firing is not expected to occur in the vicinity of the Sn particles because the liquid-phase Sn is not generated in the primary firing. Therefore, interfacial Sn wetting is considered to

Table 3 Solidus and liquidus temperatures of the Bi–Sn alloy particles used as the starting material

Particle composition		Solidus temperature (K)	Liquidus temperature (K)
Starting material particles	Bi-43 wt% Sn	411 (eutectic temp.)	411 (eutectic temp.)
	Bi-75 wt% Sn	411 (eutectic temp.)	465
	Bi-90 wt% Sn	420	489
	Sn	505 (melting point)	505 (melting point)

be limited to the Sn atoms originating from the Bi-43 wt% Sn particles, and the reinforcement of the interface will be insufficient.

Improvement of the bonding strength of the Zn-mixed hybrid joint by the reduction of the mixing ratio of Bi was achieved, and eutectic Bi-43 wt% Sn alloy was used as a trigger of Sn diffusion. However, the requirement for the use of a trigger and the optimal mixing ratio have not been verified. Therefore, further efforts are necessary to determine the optimal mixing ratio and obtain a stronger joint. Additionally, examination of the reliability of the joint is necessary to obtain improved joints.

4 Summary

The effect of the Bi–Sn composition on the bonding strength of the Zn-mixed SiC/Cu and SiC/DBC hybrid joints was examined, and the following results were obtained:

(1) The dependence of the bonding strength on the Bi–Sn composition was independent of the joint structure, and the maximum bonding strength was obtained with the average Bi fraction in the Bi–Sn alloy particles of 38.2 wt%. This composition is more Sn-rich than the eutectic Bi–Sn alloy composition. The bonding strength of the SiC/Cu joints was lower than that of the SiC/DBC joints in the entire Bi–Sn composition range.

(2) Segregation of the Bi-rich phase at the interfacial region decreased with decreasing average Bi fraction in the Bi–Sn particles. Defects such as voids and cracks were also observed in the bonding layer. The Bi segregation fraction and the number of defects were higher at the edge than in the center of the bonding region and were higher in the SiC/Cu joint than in the SiC/DBC joint.

(3) Delamination of the bonding layer at the interface was observed in the SiC/Cu joint with the average Bi fraction of 34.2 wt% (Bi-43 wt% Sn + Sn).

(4) There was little difference in the types of the constituent phases in the bonding layer between the SiC/Cu and SiC/DBC joints.

The above results indicate that higher bonding strength can be achieved by Zn mixing in the hybrid by using more Bi-rich powder than eutectic composition Bi–Sn powder. The Zn mixing enables a decrease in the Bi fraction of the Bi–Sn alloy through the activation of the migration and reaction inside of the bonding layer, which leads to the reinforcement of the interface and bonding layer, even though the bonding strength is affected by the residual stress in the bonding region.

References

1. P.G. Neudeck, R.S. Okojie, L.Y. Chen, Proc. IEEE **90**, 1065 (2002)
2. G. Liu, B.R. Tuttle, S. Dhar, Appl. Phys. Rev. **2**, 021307 (2015)
3. T. Kimoto, Jpn. J. Appl. Phys. **54**, 040103 (2015)
4. J.B. Casady, R.W. Johnson, Solid State Electron. **39**, 1409 (1996)
5. M. Willander, M. Friesel, Q.-U. Wahab, B. Straumal, J. Mater. Sci. Mater. Electron. **17**, 1 (2006)
6. C. Buttay, D. Planson, B. Allard, D. Bergogne, P. Bevilacqua, C. Jobert, M. Lazar, C. Martin, H. Morel, D. Tournier, C. Raynaud, Mater. Sci. Eng. B **176**, 283 (2011)
7. T. Laurila, V. Vuorinen, J.K. Kivilahti, Mater. Sci. Eng. R **49**, 1 (2005)
8. H. Ma, J.C. Suhling, J. Mater. Sci. **44**, 1141 (2009)
9. L. Zhang, C. He, Y. Guo, J. Han, Y. Zhang, X. Wang, Microelectron. Reliab. **52**, 559 (2012)
10. E. Ide, S. Angata, A. Hirose, K.F. Kobayashi, Acta Mater. **53**, 2385 (2005)
11. K.S. Siow, J. Electron. Mater. **43**, 947 (2014)
12. T. Ishizaki, R. Watanabe, J. Mater Chem. **22**, 25198 (2012)
13. T. Ishizaki, T. Satoh, A. Kuno, A. Tane, M. Yanase, F. Osawa, Y. Yamada, Microelectron. Reliab. **53**, 1543 (2013)
14. T. Yamakawa, T. Takemoto, M. Shimoda, H. Nishikawa, K. Shiokawa, N. Terada, J. Electron. Mater. **42**, 1260 (2013)
15. Y. Kobayashi, T. Shirochi, Y. Yasuda, T. Morita, Int. J. Adhes. Adhes. **33**, 50 (2012)
16. J. Liu, H. Chen, H. Ji, M. Li, A.C.S. Appl, Mater. Interfaces **8**, 33289 (2016)
17. J. Li, C.M. Johnson, C. Buttay, W. Sabbah, S. Azzopardi, J. Mater. Process. Technol. **215**, 299 (2015)
18. K.D. Min, K.H. Jung, C.J. Lee, H. Jeong, S.B. Jung, J. Mater. Sci. Mater. Electron. **30**, 18848 (2019)
19. N.S. Bosco, F.W. Zok, Acta Mater. **52**, 2965 (2004)
20. B.-S. Lee, S.-K. Hyun, J.-W. Yoon, J. Mater. Sci. Mater. Electron. **28**, 7827 (2017)
21. Z.-L. Li, H. Tian, H.-J. Dong, X.-J. Guo, X.-G. Song, H.-Y. Zhao, Z.-C. Feng, Scripta Mater. **156**, 1 (2018)
22. M.K. Faiz, K. Bansho, T. Suga, T. Miyashita, M. Yoshida, J. Mater. Sci. Mater. Electron. **28**, 16433 (2017)
23. F. Lang, H. Yamaguchi, H. Nakagawa, H. Sato, J. Electrochem. Soc. **160**, D315 (2013)
24. S. Fukumoto, K. Miyake, S. Tatara, M. Matsushima, K. Fujimoto, Mater. Trans. **56**, 1019 (2015)
25. Z.X. Zhu, C.C. Li, L.L. Liao, C.K. Liu, C.R. Kao, J. Alloys Compd. **671**, 340 (2016)
26. O. Mokhtari, H. Nishikawa, J. Mater. Sci.: Mater. Electron. **27**, 4232 (2016)
27. T. Satoh, T. Ishizaki, M. Usui, Mater. Des. **124**, 203 (2017)
28. P.L. Liu, J.K. Shang, Scripta Mater. **44**, 1019 (2001)
29. H.F. Zou, Q.K. Zhang, Z.F. Zhang, Scripta Mater. **61**, 308 (2009)
30. F. Wang, L. Zhou, X. Wang, P. He, J. Alloys Compd. **688**, 639 (2016)
31. Z. Wang, Q.K. Zhang, Y.X. Chen, Z.L. Song, J. Mater. Sci. Mater. Electron. **30**, 18524 (2019)
32. S. Tajima, T. Satoh, T. Ishizaki, M. Usui, J. Mater. Sci. Mater. Electron. **28**, 1764 (2017)
33. T. Satoh, T. Ishizaki, M. Usui, J. Mater. Sci. Mater. Electron. **29**, 7161 (2018)
34. T. Satoh, M. Usui, J. Mater. Sci. Mater. Electron. **29**, 20415 (2018)
35. T. Ishizaki, K. Akedo, T. Satoh, R. Watanabe, J. Electron. Mater. **43**, 774 (2014)
36. T. Satoh, T. Ishizaki, K. Akedo, J. Electron. Mater. **46**, 1279 (2017)

37. S.-M. Lee, J.-W. Yoon, S.B. Jung, J. Mater. Sci. Mater. Electron. **26**, 1649 (2015)
38. P. Villars (Chief Editor), Ag-Bi binary phase diagram 0–100 at.% Bi, in PAULING FILE in *Inorganic Solid Phases*, (Springer, Heidelberg, 2016). https://materials.springer.com/isp/phase-diagram/docs/c_0906212. Accessed 12 Apr 2017
39. K.M. Asl, J. Luo, Acta Mater. **60**, 149 (2012)
40. Y. Yanaka, Y. Kariya, H. Watanabe, H. Hokazono, Mater. Trans. **57**, 819 (2016)
41. W.H. Tao, C. Chen, C.E. Ho, W.T. Chen, C.R. Kao, Chem. Mater. **13**, 1051 (2001)
42. J. Gröbner, Bi-Sn-Zn (Bismuth-Tin-Zinc), in *Landolt-Börnstein—Group IV Physical Chemistry 11C3 (Non-Ferrous Metal Systems. Part 3)*, ed. by G. Effenberg, S. Ilyenko (Springer, Berlin, 2007). https://materials.springer.com/lb/docs/sm_lbs_978-3-540-47004-5_22. Accessed 9 July 2018
43. C. Chou, S. Chen, Acta Mater. **54**, 2393 (2006)
44. S.-W. Yoon, M.D. Glover, K. Shiozaki, I.E.E.E. Trans, Power Electron. **28**, 2448 (2013)
45. A.D. LeClaire, G. Neumann, Diffusion of impurities in solid metallic elements, in *Landolt-Börnstein—Group III Condensed Matter 26 (Diffusion in Solid Metals and Alloys)*, ed. by H. Mehrer (Springer, Berlin, 1990). https://materials.springer.com/lb/docs/sm_lbs_978-3-540-46109-8_29. Accessed 9 May 2018

Publisher's Note Springer Nature remains neutral with regard to jurisdictional claims in published maps and institutional affiliations.